SCIENTIFIC REPORTS

OPEN

Highly Efficient Photocatalytic Z-Scheme Hydrogen Production over Oxygen-Deficient WO_{3-x} Nanorods supported $Zn_{0.3}Cd_{0.7}S$ Heterostructure

Ammar Bin Yousaf [ID] [1], M. Imran[2], Syed Javaid Zaidi[1] & Peter Kasak[1]

The demand for clean renewable energy is increasing due to depleting fossil fuels and environmental concerns. Photocatalytic hydrogen production through water splitting is one such promising route to meet global energy demands with carbon free technology. Alternative photocatalysts avoiding noble metals are highly demanded. Herein, we fabricated heterostructure consist of oxygen-deficient WO_{3-x} nanorods with $Zn_{0.3}Cd_{0.7}S$ nanoparticles for an efficient Z-Scheme photocatalytic system. Our as obtained heterostructure showed photocatalytic H_2 evolution rate of 352.1 μmol h^{-1} with apparent quantum efficiency (AQY) of 7.3% at $\lambda = 420$ nm. The photocatalytic hydrogen production reaches up to 1746.8 μmol after 5 hours process in repeatable manner. The UV-Visible diffuse reflectance spectra show strong absorption in the visible region which greatly favors the photocatalytic performance. Moreover, the efficient charge separation suggested by electrochemical impedance spectroscopy and photocurrent response curves exhibit enhancement in H_2 evolution rate. The strong interface contact between WO_{3-x} nanorods and $Zn_{0.3}Cd_{0.7}S$ nanoparticles ascertained from HRTEM images also play an important role for the emigration of electron. Our findings provide possibilities for the design and development of new Z-scheme photocatalysts for highly efficient hydrogen production.

The increasing demand for energy and depleting crude oil resources forced researchers to find alternate options for rapidly growing world population. The burning of fossil fuels also deteriorating world's climate by the emission of CO_2 and other green house gases[1]. Therefore, a sustainable and clean energy source is the biggest challenge for the 21st century. Photocatalytic hydrogen production emerges as environment friendly method since the pioneer work of Fujishima and Honda in 1972[2]. Since then, a large number of photocatalysts have been synthesized for water splitting to generate hydrogen[3]. However, most of catalysts either depend upon expensive noble metals as co-catalyst (Pt, Ru, and Rh) or only absorb in the ultraviolet region which accounts for only 4% of the incoming solar light. Metal oxides such as WO_3, NiO and RuO_2 emerges as new class of photocatalyst for efficient hydrogen production[4–9]. However, photocatalysts with maximum absorption in the visible region and suitable band-gap are highly desirable.

Cadmium sulphide (CdS) attracts considerable attention due to its narrow band gap (2.4 eV) for photocatalytic hydrogen evolution reaction. However the rate of H_2 production over CdS is very low because of its photo-corrosion property and fast-recombination of electron–hole pair which renders its practical applications impossible[10]. The use of co-catalyst or incorporation of Zn ion into CdS to form $Zn_{1-x}Cd_xS$ (0–1) greatly enhances the photocatalytic activity. Recently, the band-gap for $Zn_{1-x}Cd_xS$ has been varied to achieve maximum visible absorption and greater charge separation efficiency for water splitting[11]. However, there are only few reports which suggest room temperature synthesis with excellent photocatalytic property and recyclability. Moreover, a heterostructure comprising two different photocatalysts is considered a better option compared to conventional

[1]Center for Advanced Materials, Qatar University, Doha, 2713, Qatar. [2]Hefei National Laboratory for Physical Sciences at Microscale, University of Science and Technology of China, Hefei, Anhui, 230026, PR China. Ammar Bin Yousaf and M. Imran contributed equally to this work. Correspondence and requests for materials should be addressed to A.B.Y. (email: ammar@mail.ustc.edu.cn) or P.K. (email: peter.kasak@qu.edu.qa)
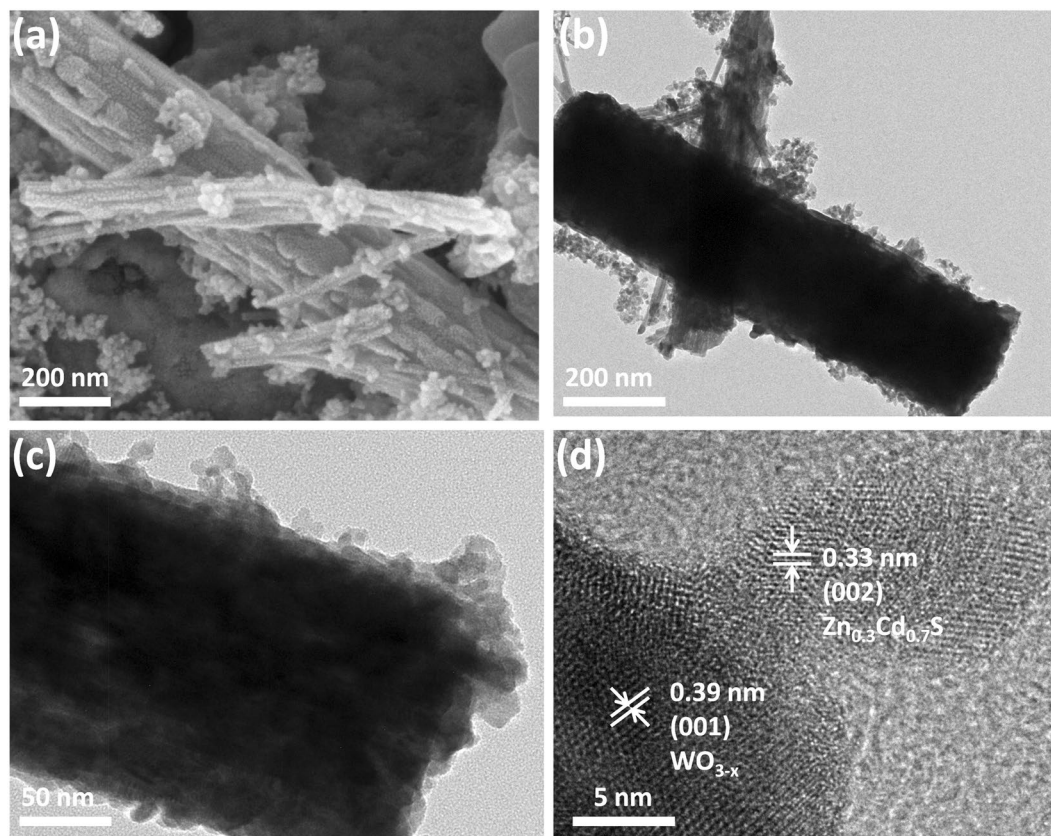
Figure 1. SEM image (**a**), TEM images (**b,c**), HRTEM images (**d**) of $WO_{3-x}/Zn_{0.3}Cd_{0.7}S$ heterostructure.

system. The Z-scheme multi-component photocatalyst system was first introduced by Bard *et al.* in 1979 based on the concept of artificial photosynthesis[12]. In multi-component Z-scheme photocatalytic system, the photogenerated electrons from Photosystem I (PSI) in the conduction band transfer through the interface contact and recombine with the photogenerated holes in the valance band of Photosystem II (PSII). This system allows the visible light to use more efficiently and dramatically improves the photocatalytic H_2 production[13].

The photocatalytic reactions are surface bound reaction, in which photogenerated electron and holes takes part in the reaction. It is well known that oxygen vacancies in a non-stoichiometric crystal also carries two electrons each which can act as double electron donor[14]. There are few recent studies in which the role of surface oxygen vacancies (SOV) was investigated thoroughly for photo-catalytic water splitting[15]. Oxygen vacancies significantly impact the electronic properties of the material and shifts absorption towards longer wavelength. Oxygen vacancies also influences magnetic[16], photocatalytic[17], optical[18], wettability[19], and electrical[20], properties of the catalyst. In a recent study, it is discovered that the oxygen vacancies improves the overall conductivity and enhances the adsorption of reactants on its surface for organic conversions[21]. Additionally, oxygen deficient metal oxide greatly enhances the visible-light driven hydrogen production by trapping the photo-induced charges and preventing the electron-hole recombination[22]. Mao and co-workers also created surface disorder in TiO_2 by hydrogenation and increased solar absorption while promoting photocatalytic activity[23]. In other recent reports, oxygen-vacancies in TiO_2, WO_3, ZnO, and Fe_2O_3 also greatly enhance photocatalytic activity[24–27].

Herein, we propose to fabricate a Z-scheme heterostructure consisting of oxygen deficient WO_{3-x} and $Zn_{0.3}Cd_{0.7}S$. Introduced oxygen vacancies in WO_3 to form $WO_{3-x}/Zn_{0.3}Cd_{0.7}S$ heterostructure significantly increases the photocatalytic hydrogen production compare to heterostructure analogue without oxygen vacancies $WO_3/Zn_{0.3}Cd_{0.7}S$. The rate of H_2 evolution for $WO_{3-x}/Zn_{0.3}Cd_{0.7}S$ heterostructure is as high as 352.1 μmol h^{-1} with apparent quantum efficiency (AQY) of 7.3% at $\lambda = 420$ nm in repeatable manner from aqueous solution containing Na_2SO_3 and Na_2S as sacrificial reagents.

Results and Discussion

The morphology, size and structure of as synthesized WO_{3-x}, $Zn_{0.3}Cd_{0.7}S$ and $WO_{3-x}/Zn_{0.3}Cd_{0.7}S$ heterostructure were analyzed by scanning electron microscopy (SEM) and transmission electron microscopy (TEM) (Fig. 1, Figs S1 and S2). As shown in Fig. S1, the $Zn_{0.3}Cd_{0.7}S$ are irregular shaped nanoparticles with a size of about 10–20 nm while the WO_{3-x} exhibit the shape of nanorods with a size in microns (Fig. S2). The SEM and TEM analysis of $WO_{3-x}/Zn_{0.3}Cd_{0.7}S$ heterostructure shows that $Zn_{0.3}Cd_{0.7}S$ nanoparticles successfully anchored on the surface of WO_{3-x} nanorods (Fig. 1). The intimate contact between WO_{3-x} and $Zn_{0.3}Cd_{0.7}S$ was observed by high resolution transmission electron microscopy (HRTEM) clearly demonstrating that $WO_{3-x}/Zn_{0.3}Cd_{0.7}S$ heterostructure with strong interface contact were successfully fabricated. The lattice spacing of 0.33 nm and 0.39 nm
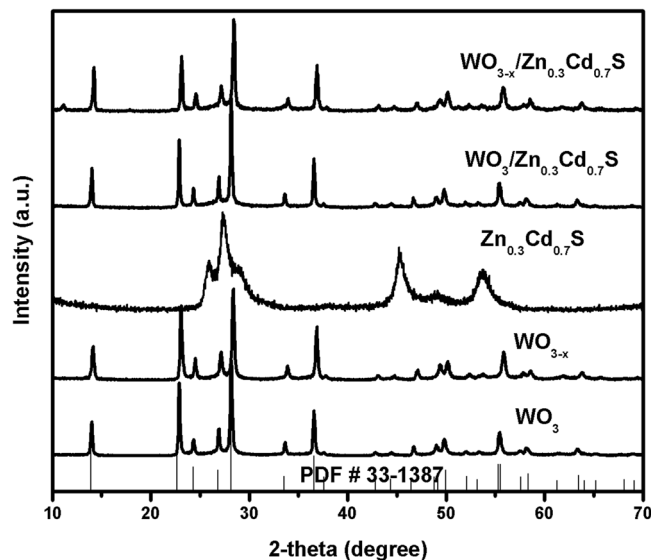
Figure 2. XRD pattern of as synthesized WO_3, WO_{3-x}, $Zn_{0.3}Cd_{0.7}S$, $WO_3/Zn_{0.3}Cd_{0.7}S$ and $WO_{3-x}/Zn_{0.3}Cd_{0.7}S$ heterostructure.
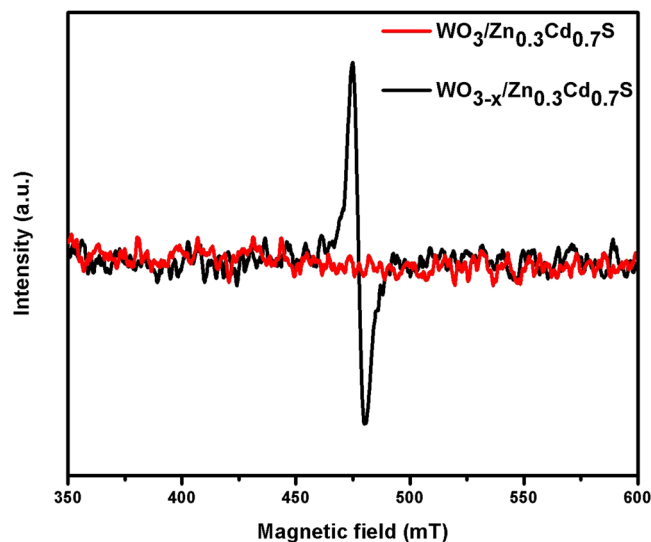
Figure 3. EPR spectra of the as synthesized $WO_3/Zn_{0.3}Cd_{0.7}S$ and $WO_{3-x}/Zn_{0.3}Cd_{0.7}S$ heterostructure recorded at $T = 130$ K.

corresponds to (002) and (001) planes of $Zn_{0.3}Cd_{0.7}S$ and WO_{3-x}, respectively, which confirms the existence of heterostructure.

The XRD patterns of as synthesized samples are shown in Fig. 2. The XRD pattern of WO_3 shows diffraction peaks which can be readily indexed to hexagonal Tungsten Oxide (JCPDS #33-1387) having cell parameters a = 7.298 Å, b = 7.298 Å, c = 3.899 Å and space group $P6/mmm$[28]. The oxygen-deficient WO_{3-x} nanorods does not shows any clear difference in XRD pattern due to large size. The characteristic XRD diffraction peaks of $Cd_{0.3}Zn_{0.7}S$ was easily observed at 28.1°, 45.7°, and 53.9° well matched with the (111), (220) and (311) planes of Zinc blend phase respectively. However, the characteristic diffraction peak of WO_3 and WO_{3-x} in $WO_3/Zn_{0.3}Cd_{0.7}S$ and $WO_{3-x}/Zn_{0.3}Cd_{0.7}S$ were not observed may be due to low content, small size of $Zn_{0.3}Cd_{0.7}S$ nanoparticles in the samples[29].

Electron paramagnetic resonance (EPR) spectra of $WO_3/Zn_{0.3}Cd_{0.7}S$ and $WO_{3-x}/Zn_{0.3}Cd_{0.7}S$ were recorded to examine the paramagnetic character. (Fig. 3) The $WO_3/Zn_{0.3}Cd_{0.7}S$ sample does not shows any signal in EPR while $WO_{3-x}/Zn_{0.3}Cd_{0.7}S$ exhibits a sharp signal at g = 2.00 which can be readily assigned as electrons trapped on oxygen vacancies, thus generating an EPR signal at g = 2.00[30].

The $Zn_{0.3}Cd_{0.7}S$ and $WO_{3-x}/Zn_{0.3}Cd_{0.7}S$ were also characterized by X-ray photoelectron spectroscopy (XPS) analysis as show in Figs 4 and S3. XPS survey spectrum of $Zn_{0.3}Cd_{0.7}S$ shown in Fig. S3 indicate the presence of Zn, Cd and S in the nanoparticles. Figure S3b shows the XPS spectrum of Zn2p with the characteristic peak at
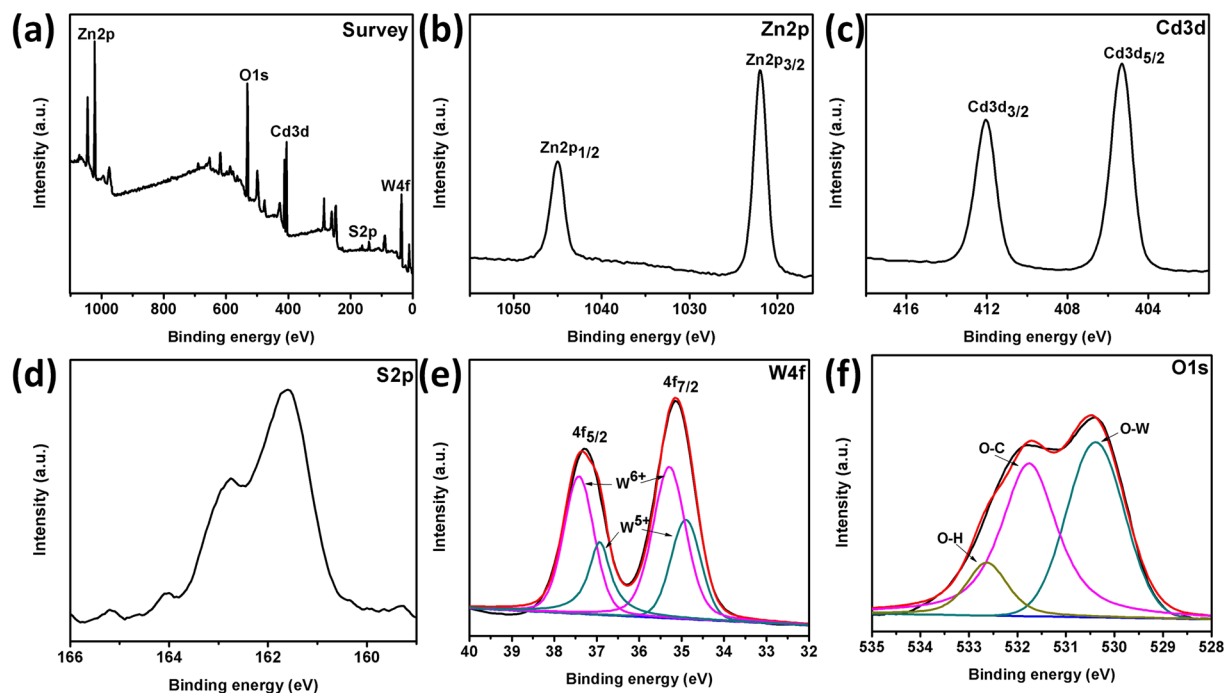
Figure 4. XPS spectra of WO_{3-x}/$Zn_{0.3}Cd_{0.7}S$ heterostructure, Survey spectrum, (**a**), Zn2p orbital (**b**), Cd3d orbital (**c**), S2p orbital (**d**), W4f orbital (**d**) and O1s orbital (**d**).

1023.6 and 1046.8 eV for $Zn2p_{3/2}$ and $Zn2p_{1/2}$, respectively. The high resolution XPS spectrum of Cd3d exhibit peaks at binding energy 405.1 and 411.8 eV corresponds to $Cd3d_{5/2}$ and $3d_{3/2}$, respectively. The S2p orbital shows a broad peak at binding energy 161.3 eV which corresponding to S^{2-}[31]. The ratio of Zn:Cd obtained from XPS analysis is well in agreement with the experimental calculations.

A typical survey XPS spectrum of WO_{3-x}/$Zn_{0.3}Cd_{0.7}S$ is also shown in Fig. 4a which confirms the coexistence of Zn, Cd, S, W, and O elements. The XPS spectra of Zn2p and Cd3d are plotted in Fig. 4b and c, respectively. The binding energies of $Zn2p_{3/2}$ and $Zn2p_{1/2}$ observed at 1021.9 and 1045.1 eV and Cd3d exhibits peaks at 405.2 eV and 412.1 eV corresponding to $Cd3d_{5/2}$ and $Cd3d_{3/2}$ respectively which agree well with the values reported for the divalent zinc and cadmium in pure metal sulphides. The S2p also show a peak at 161.5 eV which corresponds to S^{2-} in the sample[31]. (Fig. 4d) There is a difference in binding energies of Zn, Cd and S for pure $Cd_{0.3}Zn_{0.7}S$ and WO_{3-x}/$Zn_{0.3}Cd_{0.7}S$ heterostructure, which suggest the difference in valence electron density and relaxation energy after heterostructure formation. The high resolution XPS spectrum of W4f orbital shows two strong peaks corresponding to $W4f_{7/2}$ and $W4f_{5/2}$. (Fig. 4e) The peaks can be further deconvoluted into two Gaussian components. The lower binding energy components centered at 34.8 eV and 36.9 eV represent W^{5+} while higher binding energy components at 35.3 eV and 37.4 eV matched with high oxidation state of tungsten (W^{6+})[32]. The presence of W^{5+} in XPS analysis is also consistent with the EPR data showing the existence of oxygen vacancies in the sample. Figure 4f shows O1s spectrum which can be deconvoluted into three Gaussian curves centered at 530.4 eV, 531.7 eV and 532.7 eV. The low binding energy component is ascribed to the O^{2-} ions in WO_{3-x} while the components at the higher binding energy region are related to the O-C from sample holder and physisorbed water molecules[33].

Figure 5 shows UV-vis diffuse reflectance spectra of WO_3, WO_{3-x}, $Zn_{0.3}Cd_{0.7}S$ and WO_3/$Zn_{0.3}Cd_{0.7}S$ and WO_{3-x}/$Zn_{0.3}Cd_{0.7}S$ heterostructure. It can be clearly seen that WO_3 shows a white color and almost no absorption in visible region while WO_{3-x} exhibit violet color and wide absorption band extending from 440 nm to 800 nm.

Additionally, $Zn_{0.3}Cd_{0.7}S$ nanoparticles can absorb at wavelengths of about 475 nm in visible spectra which corresponds to a band gap of 2.61 eV. WO_3/$Zn_{0.3}Cd_{0.7}S$ displays a light green color, suggesting that the loading of $Zn_{0.3}Cd_{0.7}S$ nanoparticles onto WO_3 nanorods with combination with oxygen deficiency of WO_{3-x} increases the UV–visible absorption. It can be observed that oxygen deficient WO_{3-x}/$Zn_{0.3}Cd_{0.7}S$ heterostructure shows a deep brown color and strong absorption in the visible region which is beneficial for the photocatalytic performance. The WO_{3-x}/$Zn_{0.3}Cd_{0.7}S$ sample shows a larger red shift compared to WO_3/$Zn_{0.3}Cd_{0.7}S$, owing to additional oxygen vacancies, which is also in agreement with EPR data.

In addition, Transient photocurrent response curves of WO_3/$Zn_{0.3}Cd_{0.7}S$ and WO_{3-x}/$Zn_{0.3}Cd_{0.7}S$ were also examined by photoelectrochemical test device under visible range for light with irradiation ($\lambda \geq 420$ nm) using Ti foil. (see the Experimental section). As shown in Fig. 6a, the photocurrent value increases rapidly at a maximum value when the light turned on due to the separation of electron hole pairs at the heterostructure–electrolyte interface. The current value drops to zero when the light turned off, which is due to the recombination of electron-holes pairs. Notably, the WO_{3-x}/$Zn_{0.3}Cd_{0.7}S$ heterostructure shows much higher photocurrent than
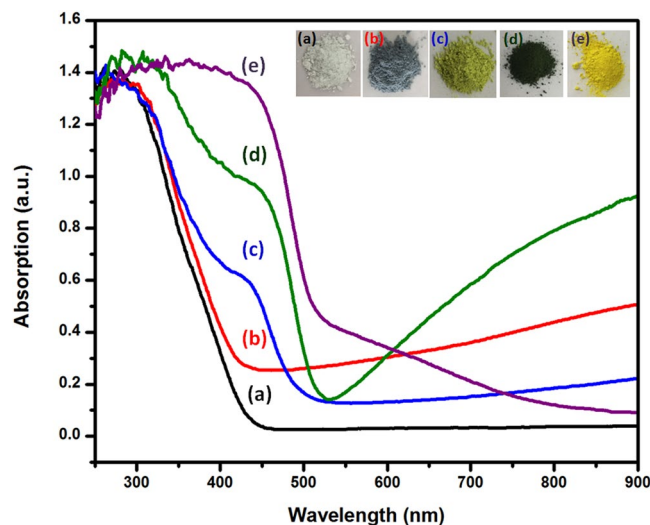
Figure 5. UV–visible diffuse reflectance spectra and inset photographs of WO_3 (**a**), WO_{3-x} (**b**), $Zn_{0.3}Cd_{0.7}S$ (**c**), $WO_3/Zn_{0.3}Cd_{0.7}S$ (**d**) and $WO_{3-x}/Zn_{0.3}Cd_{0.7}S$ heterostructure (**e**).
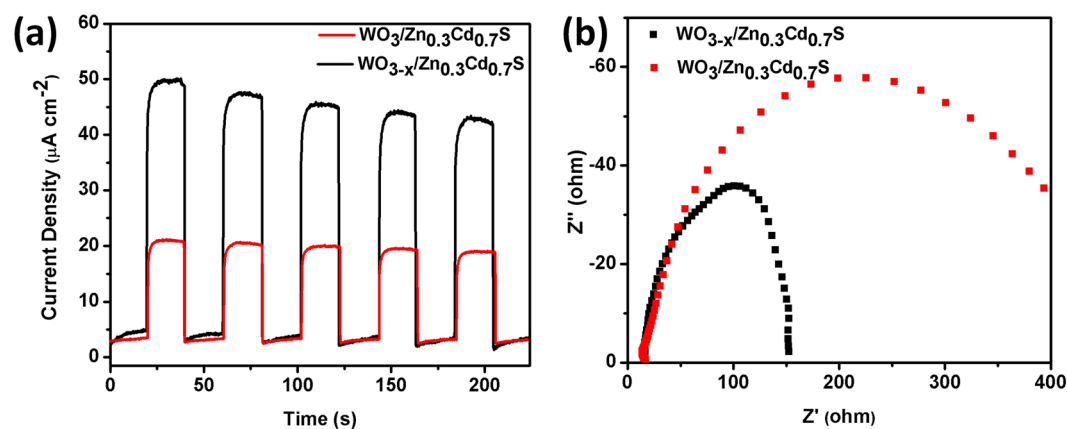
Figure 6. Photocurrent response vs. time and Nyquist plots for $WO_3/Zn_{0.3}Cd_{0.7}S$ and $WO_{3-x}/Zn_{0.3}Cd_{0.7}S$ heterostructure.

$WO_3/Zn_{0.3}Cd_{0.7}S$, suggesting that the oxygen-deficient WO_{3-x} facilitate the charge transfer process resulting in higher photocatalytic performance[34].

Electrochemical impedance spectroscopy (EIS) was also performed on a photoelectrochemical setup to investigate the charge separation efficiency of $WO_3/Zn_{0.3}Cd_{0.7}S$ and $WO_{3-x}/Zn_{0.3}Cd_{0.7}S$ heterostructure as is depicted in Fig. 6b. The large semicircle in the Nyquist plots represents the charge transfer process, while the smaller arc demonstrate fast separation of photogenerated electron–hole pairs and efficient interface charge flow[35]. As shown in Fig. 6b, the $WO_3/Zn_{0.3}Cd_{0.7}S$ have semicircle at the high frequency while $WO_{3-x}/Zn_{0.3}Cd_{0.7}S$ showed low charge transfer resistance (*Rct*) and much smaller semicircle suggesting the oxygen vacancies increase electrical conductivity and enhance visible-light driven hydrogen production[36, 37]. The oxygen vacancies thus providing a key role of rapid electron transfer for our Z-scheme photocatalytic H_2 system. The results are also consistent with photocurrent response and diffuse UV-visible reflectance data.

The photocatalytic H_2-evolution reactions of WO_3, WO_{3-x}, $WO_3/Zn_{0.3}Cd_{0.7}S$ and $WO_{3-x}/Zn_{0.3}Cd_{0.7}S$ were performed in the presence of Na_2S and Na_2SO_3 as sacrificial reagents under xenon lamp irradiation (Figure 7a). WO_3 nanorods exhibit very low H_2-evolution rate (2 μmol h^{-1}). The band edge position of γ-monoclinic phase of WO_3 is not optimal for photocatalytic water splitting, however, the band edge of hexagonal-WO_3 match up with the redox potential of water, which is used in our case and exhibit very low H_2-evolution rate while the oxygen deficient WO_{3-x} shows a better performance for H_2 production (10 μmol h^{-1}) implying the presence of oxygen vacancies leads to increase in photocatalytic activity[38]. $Zn_{0.3}Cd_{0.7}S$ nanoparticles alone showed moderate photocatalytic H_2-evolution rate (19.2 μmol h^{-1}). Remarkably, the $WO_3/Zn_{0.3}Cd_{0.7}S$ Z-scheme system showed an improvement in hydrogen production under visible light with H_2-evolution rate of 132 μmol h^{-1}. The defect rich $WO_{3-x}/Zn_{0.3}Cd_{0.7}S$ heterostructure demonstrates highest rate of H_2 production 352.1 μmol h^{-1} with apparent quantum efficiency (AQY) of 7.3% at 420 nm. The photocatalytic hydrogen production reaches up to 1746.8
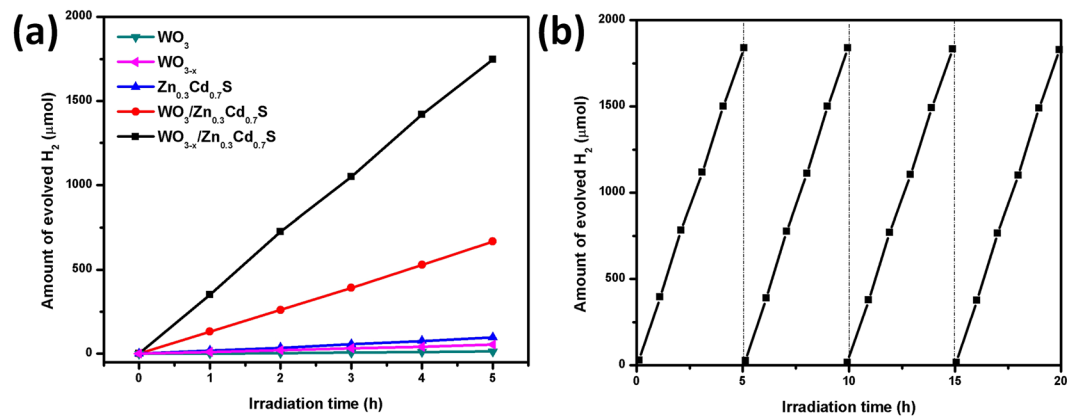
Figure 7. (**a**) Time courses of photocatalytic H_2 evolution from Na_2SO_3, Na_2S aq. solution on WO_3, WO_{3-x}, $Zn_{0.3}Cd_{0.7}S$, $WO_3/Zn_{0.3}Cd_{0.7}S$ and $WO_{3-x}/Zn_{0.3}Cd_{0.7}S$ heterostructure, (**b**) Time-cycle photocatalytic hydrogen production over $WO_{3-x}/Zn_{0.3}Cd_{0.7}S$ heterostructure under visible–light illumination ($\lambda \geq 420$ nm).

μmol in 5 h process which is considerably higher than some previous reports on photocatalytic H_2 production such as $TiO_2/Pt/P_2W_{17}$[39], $TiO_2/Au/CdS$[40], $ZnO/Au/CdS$[41], $WO_3/PbBi_2Nb_{1.9}Ti_{0.1}O_9$[42], $BiVO_4/Ru-SrTiO_3$[43] which showed rate 19.6, 3.2, 60.8, 14.8 and 22 μmol h^{-1}, respectively. It is worth mentioning that no noble metals were used in our system[44–46]. Moreover, as it is seen from Fig. 7b, the process for production is repeatable and after 4 cycles was not observed decreasing in activities confirming stability, robustness and durability of this systems. The UV-vis diffuse reflectance spectra of oxygen deficient WO_{3-x} nanorods show a prominent color change and strong absorption in the visible region which is favorable for the photocatalytic hydrogen production. The photocurrent response and EIS results also demonstrate more efficient photoelectron emigration in oxygen deficient-WO_{3-x}/ $Zn_{0.3}Cd_{0.7}S$ heterostructure compared to oxygen-vacancy-free $WO_3/Zn_{0.3}Cd_{0.7}S$ sample. The fast electron transfer efficiently captures the photo induced holes in the valence band (VB) of $Zn_{0.3}Cd_{0.7}S$. The fast recombination of e/h by the photo-generated electrons from conduction band (CB) of WO_{3-x} and holes from the VB of $Zn_{0.3}Cd_{0.7}S$ results in excellent photocatalytic performance. For our oxygen-deficient $WO_{3-x}/Zn_{0.3}Cd_{0.7}S$ Z-scheme system, the photo-generated holes tend to be present in the VB WO_{3-x}, while the electrons in the conduction band of WO_{3-x} combine with the holes of $Zn_{0.3}Cd_{0.7}S$ through the interface contact. As a result, the photo-generated charge carrier recombination can be significantly decreased. Therefore, more electrons in the CB of $Zn_{0.3}Cd_{0.7}S$ are available to reduce H^+ to H_2, which results in highly efficient H_2 production[47]. The visible light absorption can be attributed to the electron transition from the WO_{3-x} valence band to the new oxygen vacancy energy bands near Fermi level, consequently, the electronic band gap decreases. Therefore, it is possible to use less energy per time to activate the photoelectrons and thus effectively improve the carrier separation efficiency[48, 49]. Oxygen vacancies also carries two electrons each which can act as double electron donors to capture photo-generated holes and enhances the H_2 evolution performance. The strong interface contact in $WO_{3-x}/Zn_{0.3}Cd_{0.7}S$ ascertained from HRTEM images also strongly favors the efficient charge movement. We have also tested our as synthesized $WO_{3-x}/Zn_{0.3}Cd_{0.7}S$ heterostructure for photocatalytic O_2 production which shows 3.24 μmol h^{-1} (Figure S4). However, the photocatalytic O_2 production is not as high as H_2 production.

The recyclability of any materials is an important marker to which it is applicable for practical applications. It has been observed that metal sulphides usually exhibit photo-corrosion property when used for prolonged photocatalytic hydrogen production. In order to analyze the stability of our as-synthesized catalyst, we also performed time course of photocatalytic hydrogen production under similar conditions. As was mentioned previously, our Z-scheme $WO_{3-x}/Zn_{0.3}Cd_{0.7}S$ heterostructure shows excellent stability for H_2 evolution. The photo-generated electrons from WO_{3-x} and oxygen vacancies also suppress the oxidation of $Zn_{0.3}Cd_{0.7}S$, thus inhibiting the photo-corrosion property resulting in enhanced photocatalytic performance. Previous reports showed that when there are small amount of oxygen vacancies in oxygen deficient material, the defect energy level is usually below the conduction band[50]. However in our case the, the concentration of oxygen vacancies in WO_{3-x} is much higher (x = 0.4) thus the defect energy level delocalized over the conduction band. The Z-scheme electron transfer pathway needs to satisfy three conditions; i.e. PS I can only produce O_2, PS II can only produce H_2 and overall water splitting can occur in the presence of PS I and PS II. WO_3 have been reported to produce O_2 while $Zn_{1-x}Cd_xS$ have shown potential to be used for photocatalytic H_2 production[51, 52]. We have also tested photocatalytic O_2 production using $WO_{3-x}/Zn_{0.3}Cd_{0.7}S$ heterostructure which shows 3.24 μmol h^{-1} and reaches up to 15.45 μmol after 5 hours. Moreover, the defect rich $WO_{3-x}/Zn_{0.3}Cd_{0.7}S$ heterostructure also demonstrates highest rate of H_2 production 352.1 μmol h^{-1}. This indicates that the photogenerated holes in the VB of WO_{3-x} and photogenerated electrons in the CB of $Zn_{0.3}Cd_{0.7}S$ are used to oxidize and reduce water into O_2 and H_2, respectively. Meanwhile, the photogenerated electrons in the CB of WO_{3-x} recombine with the photogenerated holes in the VB of $Zn_{0.3}Cd_{0.7}S$ through the solid-solid interface contact[53]. Meanwhile, the photo-generated electrons in the conduction band of $Zn_{0.3}Cd_{0.7}S$ reduces H^+ to H_2 while the photo-generated holes in conduction band of WO_{3-x} trapped by sacrificial reagents which undergo the oxidation of SO_3^{2-} to SO_4^{2-}[54] (Figure 8). This possible Z-scheme mechanism is also consistent with the experimental data, EIS and transient photocurrent response
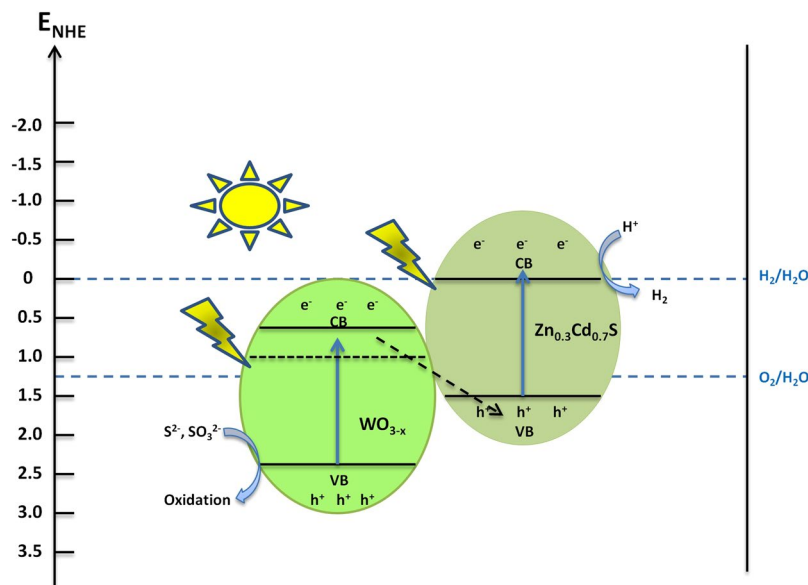
Figure 8. A schematic presentation of the charge transfer process for $WO_{3-x}/Zn_{0.3}Cd_{0.7}S$ heterostructure.

results and various previous reports[55–59]. Our multi-component Z-scheme system provides advancement in the design and development of low-cost highly efficient photocatalytic materials for water splitting.

Conclusions

In conclusion, we have synthesized a unique no noble metal Z-scheme photocatalyst by fabrication of oxygen-deficient WO_{3-x} nanorods with $Zn_{0.3}Cd_{0.7}S$ nanoparticles. The $WO_{3-x}/Zn_{0.3}Cd_{0.7}S$ heterostructure shows visible light driven hydrogen production of 352.1 μmol h^{-1} with apparent quantum efficiency (AQY) of 7.3% at 420 nm. The photocatalytic H_2 evolution reaches up to 1746.8 μmol after 5 hours in repeatable manner without decreasing activites over 4 cycles. The EIS and photocurrent response results suggest efficient charge separation which is key factor for the enhancement of the activity. The solid-solid interfacial contact between WO_{3-x} and $Zn_{0.3}Cd_{0.7}S$ favors photo-generated electron emigration from the conduction band of WO_{3-x} to the valance band of $Zn_{0.3}Cd_{0.7}S$, thus capturing the photogenerated holes. The remaining photogenerated electrons in the conduction band of $Zn_{0.3}Cd_{0.7}S$ efficiently reduce H^+ to H_2. Overall the hydrogen evolution rate over oxygen-deficient $WO_{3-x}/Zn_{0.3}Cd_{0.7}S$ heterostrcture is considerably high compared to $WO_3/Zn_{0.3}Cd_{0.7}S$ and without the use of noble metals. Our approach opened up new avenue for to synthesis Z-scheme photocatalytic system for efficient hydrogen production from water splitting.

Experimental

Chemicals.   Sodium tungstate (Na_2WO_4), Sodium sulfate (Na_2SO_4), Zinc acetate ($Zn(CH_3COO)_2 \cdot 2H_2O$), Cadmium acetate ($Cd(CH_3COO)_2 \cdot 2H_2O$), Sodium sulfide nonahydrate ($Na_2S \cdot 9H_2O$), Sodium sulphite (Na_2SO_3) were purchased from Sinopharm Chemical Reagent. All other chemical reagents were of analytical grade and used as received without further purification.

Characterization.   The morphology of the particles was observed by scanning electron microscope (SEM, JSM 6700F, JEOL). Transmission electron microscopic (TEM) images and high-resolution transmission electron microscopic (HRTEM) images were carried out on a JEM-2100F field emission electron microscope at an accelerating voltage of 200 kV. The X-ray powder diffraction (XRD) patterns of the products were performed on a Philips X'Pert Pro Super diffractometer with Cu-Kα radiation ($\lambda = 1.54178$ Å). The operation voltage was maintained at 40 kV and current at 200 mA, respectively. The X-ray photoelectron spectroscopy (XPS) was carried out on a PerkinElmer RBD upgraded PHI-5000C ESCA system. A Shimadzu spectrophotometer (Model 2501 PC) was used to record the UV–vis diffuse reflectance spectra of the samples in the region of 200 to 800 nm. The electron paramagnetic resonance (EPR) spectra were recorded on a JEOL JES-FA200 EPR spectrometer (140 K, 9064 MHz, 0.998 mW, X-band).

Synthesis.   Heterostructure $WO_{3-x}/Zn_{0.3}Cd_{0.7}S$ was synthesized in simple three steps. In the first hexagonal WO_3 nanorods were prepared by hydrothermal reaction. Subsequently calcination in Ar/H_2 environment was carried out to results WO_{3-x}. Finally $Zn_{0.3}Cd_{0.7}S$ was introduced to nanorod surface by reaction of Zn^{2+}, Cd^{2+} precursors and Na_2S in alkali conditions. Detailed synthesis is as follows:

Synthesis of WO_{3-x} Nanorods. WO_{3-x} nanorods were synthesized by adding 0.1 g of Sodium tungstate and 0.05 g of Sodium sulfate in 4 ml of water followed by drop wise addition of 0.5 M HCl to adjust the pH value of the solution to 2.0. Then, the solution was poured into Teflon-lined stainless steel autoclave and heated 190 °C for 24 h. After cooling down the autoclave, the products was obtained by centrifugation and washed thoroughly with

water, ethanol and dried at 60 °C. The centrifuge material was further treated for calcinations in a furnace for 2 h at 350 °C in Ar/H$_2$ environment (10 mL min^{-1}) with heating rate of 5 °C min^{-1}. The final product obtained was further used for characterizations, heterostructure synthesis and applications. The synthesis of WO$_3$ nanorods was same except the calcinations process.

Synthesis of WO$_{3-x}$/Zn$_{0.3}$Cd$_{0.7}$S Heterostructure.

In a typical synthesis, 50 mg WO$_{3-x}$ nanorods were dispersed in 100 mL of distilled water, then a certain amount of Zn(CH$_3$COO)$_2$·2H$_2$O and Cd(CH$_3$COO)$_2$·2H$_2$O were added and pH of the solution was adjusted to 7.4 using 0.1 M sodium hydroxide. After 10–15 minutes, aqueous solution of sodium sulfide (Na$_2$S . 9H$_2$O) was drop wise added into above solution. The resultant mixture was stirred at room temperature for 24 h. The obtained powders were washed with water and ethanol and dried in oven at 60 °C. The Synthesis of WO$_3$/Zn$_{0.3}$Cd$_{0.7}$S heterostructure was same and bare Zn$_{0.3}$Cd$_{0.7}$S nanoparticles were also prepared following the same procedure except the use of WO$_{3-x}$. The optimum ratio of WO$_3$, WO$_{3-x}$ and Zn$_{0.3}$Cd$_{0.7}$S in WO$_3$/Zn$_{0.3}$Cd$_{0.7}$S, and WO$_{3-x}$/Zn$_{0.3}$Cd$_{0.7}$S heterostructure was obtained to be 1:1.2 and 1:1.2, respectively.

Photocatalytic reaction.

The photocatalytic H$_2$ evolution from water splitting was performed in a vacuumed, gas–closed circulation system using 300 W Xe lamp equipped with a $\lambda \geq 420$ nm cut–off filter. The average light intensity was 2.84 mW/cm^2. In a typical procedure, 100 mg of catalyst was dispersed in 100 mL water containing 0.1 M Na$_2$S and 0.1 M Na$_2$SO$_3$. The on–line gas chromatography (Agilent, 6820, TCD detector, N$_2$ carrier) was used to determine the amount of hydrogen evolved and compared with other samples. The photocatalytic O$_2$ production performed vacuumed, gas–closed circulation system in 5 mM KIO$_3$ solution using 300 W Xe lamp equipped with a $\lambda \geq 420$ nm cut–off filter. The on–line gas chromatography (Agilent, 6820, TCD detector, N$_2$ carrier) was used to determine the amount of oxygen evolved.

Quantum efficiency measurement.

Apparent quantum yields (AQYs) were determined using a 420 nm band pass filter. The number of incident photons from the Xenon lamp were measured with a power meter (1831-R, Newport). Apparent quantum yields (AQYs) were calculated by the following equation:

$$AQY\ (\%) = \frac{2 \times The\ number\ of\ evolved\ H_2\ molecules}{The\ number\ of\ incident\ photons} \times 100$$

Electrochemical and Photo-electrochemical measurements.

Electrochemical and photoelectrochemical measurements were conducted in 0.1 M Na$_2$SO$_4$ electrolyte solution with a three-electrode quartz cell. Ag/AgCl was used as reference electrode while platinum wire was used as counter electrode and catalysts film electrodes on Ti foil worked as working electrode. The catalysts films were prepared by dropping catalyst suspensions (10 mg mL^{-1} in ethanol) onto Ti foil by following doctor-blade coating method with a glass rod and scotch tape and resultant electrodes were annealed for 12 h at 90 °C. For the measurements, the electrodes were pressed against an electrochemical cell with a working area of 4.0 cm^2. Photo-electrochemical test systems were composed of a CHI 660B electrochemistry potentiostat (Shanghai Chenhua Limited, China).

References

1. Ni, M., Leung, M. K. H., Leung, D. Y. C. & Sumathy, K. A Review and Recent Developments in Photocatalytic Water–Splitting using TiO$_2$ for Hydrogen Production. *Renew. Sust. Energ. Rev.* **11**, 401–425 (2007).
2. Fujishima, A. & Honda, K. Electrochemical Photolysis of Water at a Semiconductor Electrode. *Nature* **238**, 37–38 (1972).
3. Hoffmann, M. R., Martin, S. T., Choi, W. & Bahnemann, D. W. Environmental Applications of Semiconductor Photocatalysis. *Chem. Rev.* **95**(1), 69–96 (1995).
4. Abe, R., Sayama, K. & Arakawa, H. Significant Effect of Iodide Addition on Water Splitting into H$_2$ and O$_2$ over Pt–loaded TiO$_2$ Photocatalyst: Suppression of Backward Reaction. *Chem. Phys. Lett.* **371**, 360–364 (2003).
5. Sato, J. *et al*. RuO$_2$-Loaded β- Ge$_3$N$_4$ as a Non-Oxide Photocatalyst for Overall Water Splitting. *J. Am. Chem. Soc.* **127**, 4150–4151 (2005).
6. Iwashina, K. & Kudo, A. Rh-Doped SrTiO$_3$ Photocatalyst Electrode Showing Cathodic Photocurrent for Water Splitting under Visible–Light Irradiation. *J. Am. Chem. Soc.* **133**, 13272–13275 (2011).
7. Hwang, D. W., Kim, J., Park, T. J. & Lee, J. S. Mg–Doped WO$_3$ as a Novel Photocatalyst for Visible Light–Induced Water Splitting. *Catal. Lett.* **80**, 53–57 (2002).
8. Kato, H. & Kudo, A. Water Splitting into H$_2$ and O$_2$ on Alkali Tantalate Photocatalysts ATaO$_3$ (A = Li, Na, and K). *J. Phys. Chem. B* **105**, 4285–4292 (2001).
9. Maeda, K., Saito, N., Lu, D. L., Inoue, Y. & Domen, K. Photocatalytic Properties of RuO$_2$-Loaded β-Ge$_3$N$_4$ for Overall Water Splitting. *J. Phys. Chem. C* **111**, 4749–4755 (2007).
10. Zong, X. *et al*. Enhancement of Photocatalytic H$_2$ Evolution on CdS by Loading MoS$_2$ as Cocatalyst under Visible Light Irradiation. *J. Am. Chem. Soc.* **130**, 7176–7177 (2008).
11. Hsu, Y. Y. *et al*. Heterojunction of Zinc Blende/Wurtzite in Zn$_{1-x}$Cd$_x$S Solid Solution for Efficient Solar Hydrogen Generation: X−ray Absorption/Diffraction Approaches. *ACS Appl. Mater. Interfaces* 7, 22558–22569 (2015).
12. Allen, J. B. Photoelectrochemistry and heterogeneous photo-catalysis at semiconductors. *J. Photochem.* **10**, 59–75 (1979).
13. Li, H. J., Tu, W. G., Zhou, Y. & Zou, Z. G. Z-Scheme Photocatalytic Systems for Promoting Photocatalytic Performance: Recent Progress and Future Challenges. *Adv. Sci.* **3**, 1500389 (2016).
14. Zou, X. X. *et al*. Facile Synthesis of Thermal and Photostable Titania with Paramagnetic Oxygen Vacancies for Visible-Light Photocatalysis. *Chem. – Eur. J.* **19**, 2866–2873 (2013).
15. Pan, X. Y., Yang, M. Q., Fu, X. Z., Zhang, N. & Xu, Y. J. Defective TiO$_2$ with oxygen vacancies: synthesis, properties and photocatalytic applications. *Nanoscale* **5**, 3601–3614 (2013).
16. Mal, S., Nori, S., Narayan, J. & Prater, J. T. Defect-mediated ferromagnetism and controlled switching characteristics in ZnO. *J. Mater. Res.* **26**, 1298–1308 (2011).
17. Bayati, M. R., Ding, J., Lee, Y. F., Narayan, R. J. & Narayan, J. Defect mediated photocatalytic decomposition of 4-chlorophenol on epitaxial rutile thin films under visible and UV illuminations. *J. Phys. C: Solid State Phys.* **24**, 395005 (2012).

18. Bayati, M. R., Joshi, S., Narayan, R. J. & Narayan, J. Low temperature processing and control of structure and properties of epitaxial TiO$_2$/Sapphire thin film heterostructures. *J. Mater. Res.* **28**, 1669–1679 (2013).

19. Bayati, M. R., Joshi, S., Molaei, R., Narayan, R. J. & Narayan, J. Ultrafast switching in wetting properties of TiO$_2$/YSZ/Si (001) heteroepitaxy induced by laser irradiation. *J. Appl. Phys.* **113**, 063706 (2013).

20. Gupta, P., Dutta, T., Mal, S. & Narayan, J. Controlled p-type to n-type conductivity transformation in NiO thin films by ultraviolet-laser irradiation. *J. Appl. Phys.* **111**, 013706 (2012).

21. Yu, H. W. *et al.* Structure–activity relationships of Cu–ZrO$_2$ catalysts for CO$_2$ hydrogenation to methanol: interaction effects and reaction mechanism. *RSC Adv.* **7**, 8709–8717 (2017).

22. Vitaly, G., Su, C. Y. & Perng, T. P. Surface reconstruction, oxygen vacancy distribution and photocatalytic activity of hydrogenated titanium oxide thin film. *J. Catal.* **330**, 177–186 (2015).

23. Chen, X., Liu, L., Yu, P. Y. & Mao, S. S. Increasing Solar Absorption for Photocatalysis with Black Hydrogenated Titanium Dioxide Nanocrystals. *Science* **331**, 746–750 (2011).

24. Wang, Z. *et al.* Visible-Light Photocatalytic, Solar Thermal, and Photoelectrochemical Properties of Aluminium-Reduced Black Titania. *Energy Environ. Sci.* **6**, 3007–3014 (2013).

25. Liu, G. *et al.* Enhancement of Visible-Light-Driven O$_2$ Evolution from Water Oxidation on WO$_3$ Treated with Hydrogen. *J. Catal.* **307**, 148–152 (2013).

26. Lv, Y. *et al.* The Surface Oxygen Vacancy Induced Visible Activity and Enhanced UV Activity of a ZnO$_{1−x}$ Photocatalyst. *Catal. Sci. Technol.* **3**, 3136–3146 (2013).

27. Ling, Y. *et al.* The Influence of Oxygen Content on the Thermal Activation of Hematite Nanowires. *Angew. Chem., Int. Ed.* **51**, 4074–4079 (2012).

28. Her, Y. C. & Chang, C. C. Facile synthesis of one-dimensional crystalline/amorphous tungsten oxide core/shell heterostructures with balanced electrochromic properties. *CrystEngComm.* **16**, 5379–5386 (2014).

29. Akhtar, M. S., Malik, M. A., Riaz, S. & Naseem, S. Room temperature ferromagnetism and half metallicity in nickel doped ZnS: Experimental and DFT studies. *Mater. Chem. Phys.* **160**, 440–446 (2015).

30. Nakamura, I. *et al.* Role of oxygen vacancy in the plasma-treated TiO$_2$ photocatalyst with visible light activity for NO removal. *J. Mol. Catal. A: Chem.* **161**, 205–212 (2000).

31. Xu, X. *et al.* Novel mesoporous Zn$_x$Cd$_{1−x}$S nanoparticles as highly efficient photocatalysts. *Appl. Catal. B: Environ.* **125**, 11–20 (2012).

32. Zhu, J. *et al.* Intrinsic Defects and H Doping in WO$_3$. *Sci. Rep.* **7**, 40882 (2017).

33. Pavel, V. K. *et al.* XPS study of surface chemistry of tungsten carbides nanopowders produced through DC thermal plasma/hydrogen annealing process. *Appl. Surf. Sci.* **339**, 46–54 (2015).

34. Zhou, X. *et al.* New Co(OH)$_2$/CdS nanowires for efficient visible light photocatalytic hydrogen production. *J. Mater. Chem. A* **4**, 5282–5287 (2016).

35. Ye, R. Q. *et al.* Fabrication of CoTiO$_3$/g-C$_3$N$_4$ Hybrid Photocatalysts with Enhanced H$_2$ Evolution: Z-Scheme Photocatalytic Mechanism Insight. *ACS Appl. Mater. Interfaces* 8, (13879–13889 2016).

36. Wang, Q. *et al.* Scalable water splitting on particulate photocatalyst sheets with a solar-to-hydrogen energy conversion efficiency exceeding 1%. *Nat. Mater.* **15**, 611–615 (2016).

37. Yang, T. H. *et al.* High Density Unaggregated Au Nanoparticles on ZnO Nanorod Arrays Function as Efficient and Recyclable Photocatalysts for Environmental Purification. *Small* **9**, 3169–3182 (2013).

38. Lee, T. H., Lee, Y. H., Jang, W. S. & Aloysius, S. Understanding the advantage of hexagonal WO$_3$ as an efficient photoanode for solar water splitting: a first-principles perspective. *J. Mater. Chem. A* **4**, 11498–11506 (2016).

39. Ning, F. N., Jin, Z. J., Wu, Y. Q., Lu, G. Q. & Li, D. Y. Z-Scheme Photocatalytic System Utilizing Separate Reaction Centers by Directional Movement of Electrons. *J. Phys. Chem. C* **115**, 8586–8593 (2011).

40. Ding, L. *et al.* Butterfly wing architecture assisted CdS/Au/TiO$_2$ Z-scheme type photocatalytic water splitting. *Int. J. Hydrogen Energ.* **38**, 8244–8253 (2013).

41. Yu, Z. B. *et al.* Self-assembled CdS/Au/ZnO heterostructure induced by surface polar charges for efficient photocatalytic hydrogen evolution. *J. Mater. Chem. A* **1**, 2773–2776 (2013).

42. Kim, H. G. *et al.* Photocatalytic ohmic layered nanocomposite for efficient utilization of visible photons. *Appl. Phys. Lett.* **89**, 64101–64103 (2006).

43. Sasaki, Y., Nemoto, H., Saito, K. & Kudo, A. Solar Water Splitting Using Powdered Photocatalysts Driven by Z-Schematic Interparticle Electron Transfer without an Electron Mediator. *J. Phys. Chem. C* **113**, 17536–17542 (2009).

44. Liu, C., Tang, J. Y., Chen, H. M., Liu, B. & Yang, P. D. A Fully Integrated Nanosystem of Semiconductor Nanowires for Direct Solar Water Splitting. *Nano Lett.* **13**, 2989–2992 (2013).

45. Hidehisa, H., Takanori, I., Shintaro, I. & Tatsumi, I. Long-time charge separation in porphyrin/KTa(Zr)O$_3$ as watersplitting photocatalyst. *Phys. Chem. Chem. Phys.* **13**, 18031–18037 (2011).

46. Ma, S. S. K. *et al.* A Redox-Mediator-Free Solar-Driven Z-Scheme Water-Splitting System Consisting of Modified Ta$_3$N$_5$ as an Oxygen-Evolution Photocatalyst. *Chem. Eur. J.* **19**, 7480–7486 (2013).

47. Yu, J. G., Wang, S. H., Low, J. X. & Xiao, W. Enhanced photocatalytic performance of direct Z-scheme g-C$_3$N$_4$–TiO$_2$ photocatalysts for the decomposition of formaldehyde in air. *Phys. Chem. Chem. Phys.* **15**, 16883–16890 (2013).

48. Dong, L. P., Jia, R. X., Xin, B., Peng, B. & Zhang, Y. M. Effects of oxygen vacancies on the structural and optical properties of β-Ga$_2$O$_3$. *Sci Rep.* **7**, 40160 (2017).

49. Gan, J. Y. *et al.* Oxygen vacancies promoting photoelectrochemical performance of In$_2$O$_3$ nanocubes. *Sci Rep.* **3**, 1021 (2013).

50. Zheng, Y. H. *et al.* Luminescence and Photocatalytic Activity of ZnO Nanocrystals: Correlation between Structure and Property. *Inorg. Chem.* **46**, 6675–6682 (2007).

51. Wang, Y. L. *et al.* Controllable Synthesis of Hexagonal WO$_3$ Nanoplates for Efficient Visible-Light-Driven Photocatalytic Oxygen Production. *Chem. Asian J.* **12**, 387–391 (2017).

52. Li, Q. *et al.* Zn$_{1−x}$Cd$_x$S Solid Solutions with Controlled Bandgap and Enhanced Visible-Light Photocatalytic H$_2$-Production Activity. *ACS Catal.* **3**, 882–889 (2013).

53. Zhou, P., Yu, J. G. & Mietek, J. All-Solid-State Z-Scheme Photocatalytic Systems. *Adv. Mater.* **26**, 4920–4935 (2014).

54. Wang, X. W. *et al.* TiO$_2$ films with oriented anatase {001} facets and their photoelectrochemical behavior as CdS nanoparticle sensitized photoanodes. *J. Mater. Chem.* **21**, 869–873 (2011).

55. Yu, W. L., Xu, D. F. & Peng, T. Y. Enhanced photocatalytic activity of g-C$_3$N$_4$ for selective CO$_2$ reduction to CH$_3$OH via facile coupling of ZnO: a direct Z-scheme mechanism. *J. Mater. Chem. A* **3**, 19936–19947 (2015).

56. Jin, J., Yu, J. G., Gu, D. P., Cui, C. & Ho, W. K. A Hierarchical Z-Scheme CdS–WO$_3$ Photocatalyst with Enhanced CO$_2$ Reduction Activity. *Small* **11**, 5262–5271 (2015).

57. Pan, L. *et al.* Highly efficient Z-scheme WO$_{3−x}$ quantum dots/TiO$_2$ for photocatalytic hydrogen generation. *Chin. J. Catal.* **38**, 253–259 (2017).

58. Cui, L. F. *et al.* Facile preparation of Z-scheme WO$_3$/g-C$_3$N$_4$ composite photocatalyst with enhanced photocatalytic performance under visible light. *Appl. Surf. Sci.* **391**, 202–210 (2017).

59. Liu, J. J., Cheng, B. & Yu, J. G. A new understanding of the photocatalytic mechanism of the direct Z-scheme g-C$_3$N$_4$/TiO$_2$ heterostructure. *Phys. Chem. Chem. Phys.* **18**, 31175–31183 (2016).

Acknowledgements

Author Contributions

M.I. and A.B.Y. conceived the idea of the synthesis method and performed the synthesis, measurement and characterizations. S.J.Z. evaluated data. P.K. evaluated data and revised the manuscript. M.I. wrote the first version of the manuscript and all authors discussed the results and contributed to the final version of the paper.

Additional Information

Supplementary information accompanies this paper at doi:10.1038/s41598-017-06808-6

Competing Interests: The authors declare that they have no competing interests.

Publisher's note: Springer Nature remains neutral with regard to jurisdictional claims in published maps and institutional affiliations.